Supporting Information

The A39G FF Domain Folds on a Volcano-shaped Free Energy Surface via Separate Pathways

Table of Contents

SI Text

A brief description of CEST.

The interested reader is referred to the original literature (1, 2) as well as a review article (3) that outlines the physical basis of the CEST approach for studying sparse protein states and to the original description of magnetization transfer due to chemical exchange in the presence of radio frequency fields by Forsen and Hoffman (4). In order to understand how the CEST experiment detects 'invisible' states we consider a simple two-site interconversion, $A \underset{k_{BA}}{\overset{k_{AB}}{\rightleftarrows}} B$, where k_{AB} and k_{BA} are forward and reverse rate constants, $k_{ex,AB} = k_{AB} + k_{BA}$, and the fractional population of state B is $p_B = k_{AB}/k_{ex,AB}$, with $p_A + p_B = 1$. Typically, $p_B << 1$ making it the 'invisible' minor state. We denote the chemical shifts (ppm) of an exchanging spin in each state as ϖ_A (state A) and ϖ_B (state B). Central to the CEST experiment is the application of a weak B_1 field (~5-50 Hz), typically at one irradiation frequency per experiment, 'searching' for the resonance position of the spin in state B. At the start of the experiment the magnetization for spins A and B is aligned along the Z-axis. However, when the irradiation frequency of the weak B_1 field, ϖ, is coincident with ϖ_B, spins in molecules in state B precess around B_1 and will not be aligned along Z when the molecule returns to state A. Additionally, during this interval magnetization is transferred from A to B and for saturating B_1 fields magnetization does not return coherently to A. The net effect is a loss of magnetization in state A. As the molecules exchange between A and B during a relaxation period of duration T_{EX} which is typically several hundreds of milliseconds the loss in magnetization can be substantial (2, 5) and the CEST profile, $I(\varpi)/I_0$ *vs* ϖ, where $I(\varpi)$ and I_0 are the intensities of the signal derived from state A with and without application of the B_1 field during the relaxation delay (T_{EX}), contains dips at both ϖ_A and ϖ_B. By analyzing CEST profiles recorded with different B_1 values, the exchange parameters $k_{ex,AB}$ and p_B can be obtained in addition to ϖ_B. CEST experiments have typically been used to study exchange reactions occurring with rate constants between ~5 to ~500 s^{-1} though faster exchange processes between the major and minor state have been studied using higher B_1 fields (6, 7).

How robust is the four-state model?

We have tested the robustness of the results from the four-state analysis of our CEST data by randomly discarding ~30% of the ^{15}N CEST profiles during the fitting process, *SI Appendix* Figure S2 ("dropout" analysis). This procedure was repeated 200 times and the data was fit to a four-state model where all four states exchange with each other and where $R_{2I1} = R_{2I2} = R_{2F}$ and $R_{2U} = R_{2F}/2$. With the exception of $k_{ex,FU}$ and $k_{ex,FI1}$ the fitting parameters are distributed around a single value. However, in the case of $k_{ex,FU}$, we obtained $k_{ex,FU}$ ~0 s^{-1} for ~90% of the trials, while $k_{ex,FU}$ ~35 s^{-1} for the remaining 10%, accompanied by a decrease in $k_{ex,FI1}$ from ~160 s^{-1} to ~40 s^{-1} such that $k_{ex,FU}$ and $k_{ex,FI1}$ are anti-correlated. As U and I1 rapidly interconvert with each other and $k_{ex,I1U} >> k_{ex,FU}$, $k_{ex,FI1}$, the ^{15}N CEST data cannot be used to distinguish which of I1 or U directly exchanges with F (χ^2_{red}=0.9 for both sets of $k_{ex,FU}$ and $k_{ex,FI1}$ values listed above).

Fits of both models ($k_{ex,FU}$ = 0 and 35 s^{-1}) to the ^{15}N CEST data result in essentially the same populations (p_{I1} 0.34 *vs* 0.32% , p_{I2} 0.19 *vs* 0.19 % and p_U 1.03 *vs* 1.04 % and chemical shifts for the I1, I2 and U states, *SI Appendix*, Fig. S2); the conclusions of our study are not affected by which set of exchange parameters is chosen. We prefer the solution with $k_{ex,FU}$ = 0 s^{-1} since the folding model is then simpler, the quality of the fits are the same (χ^2_{red}=0.9 for both models, *SI Appendix* Table S2) and because every other FF variant studied folds via an intermediate (8-10). Further in regular Monte-Carlo and bootstrap protocols in which entire ^{15}N CEST profiles were not discarded, $k_{ex,FU}$ and $k_{ex,FI1}$ are well defined with ~99% of the values around ~0 and ~160 s^{-1} respectively.

As discussed in the main text, Ser 56 is the only residue for which a distinct I2 state dip was observed in ^{15}N CEST profiles. Therefore, we wanted to verify that the selected four-state folding model was not biased by the fortuitously large $\Delta\varpi_{FI2}$ value for this one residue. A general three-state model where F, I and U interconvert with each other, subject to the constraints R_{2I} =R_{2F} and R_{2U} =R_{2F}/2, did not fit the ^{15}N CEST data well, even when Ser 56 was removed (χ^2_{red}~ 1.67, *SI Appendix* Table S2), though the fits were worse when Ser 56 was included (χ^2_{red}~ 2.44, *SI Appendix* Table S2). Not constraining R_{2U} in a dataset where Ser 56 was removed improves the quality of the fits (χ^2_{red}~ 1.0, *SI Appendix* Table S2), yet R_{2U} rates for a significant number of residues were > 100 s^{-1} indicating that the unfolded state exchanges with an additional conformer that is not within the model and that Ser 56 is not biasing this conclusion. Without Ser 56 the F ↔ I2 ↔ I1 ↔ U model fit the ^{15}N CEST data well (χ^2_{red}~ 0.93, *SI Appendix* Table S2) even with the constraints R_{2I1} = R_{2I2} = R_{2F} and R_{2U} = R_{2F}/2, although the I2 ↔ F ↔ I1 ↔ U model did not (χ^2_{red}~ 1.47, *SI Appendix* Table S2). Thus the requirement of a four-state model to fit the data is not dependent on whether Ser 56 is included in the analysis. However, Ser 56 is required for the selection of the 'correct' four-state model (*i.e.*, to distinguish between different four-state models, Fig. 3).

Materials and Methods

Protein expression and purification. WT, A17G, and A39G FF domains were overexpressed in *E coli* BL21(DE3) cells transformed with pET-29b plasmids containing the appropriate genes (Genscript). [U -^{15}N] protein was expressed in cells grown in M9 media with 1 g/l $^{15}NH_4Cl$ as the nitrogen source and purified using a two-step protocol consisting of a cation exchange (5 ml SP Fast Flow, GE) step followed by size exclusion (120 ml Superdex 75, GE) chromatography as described previously (11).

NMR samples. The ~550 µl NMR samples contained ~2 mM [U- ^{15}N] protein dissolved in the appropriate buffer (*SI Appendix* Table S1). In the A39G FF sample used to study four-state exchange (Sample 1, *SI Appendix* Table S1) the fraction of added D_2O for the lock was limited to 2.5% to avoid complications due to H/D exchange during the T_{EX} period (12).

NMR spectroscopy. NMR experiments were performed on Bruker Avance III HD (600 & 700 MHz) and Neo (500 MHz & 1 GHz) spectrometers equipped with triple resonance cryogenically cooled (600 MHz, 700 MHz & 1 GHz) or room temperature probes (500 MHz), with X, Y, Z (600 MHz & 1 GHz) or Z (500 MHz & 700 MHz) gradients. Amide ^{15}N CEST data was recorded using the standard ^{15}N CEST sequence (1) in which the ^{15}N-^{1}H spin system is essentially reduced to an isolated spin ½ spin system by ^{1}H decoupling using 90x240y90x composite inversion pulses (13) during the exchange period of duration T_{EX}. To expedite data acquisition, 24 to 30 complex data points were recorded in the indirect ^{15}N dimension with a sweep width of 16.9 ppm. The ^{15}N B_1 field was calibrated using the nutation method (14). Additional details are listed in *SI Appendix* Table S1. The D-CEST experiment (15, 16) was not used to record ^{15}N CEST profiles as decoupling artifacts can alias into the region of interest.

Data analysis. The *NMRPipe* software package was used to processes the NMR data (17), *SPARKY* (18, 19) to visualize and label the spectra, and *PINT* (20) to extract peak intensities from the two-dimensional ^{1}H-^{15}N planes in the CEST datasets. *ChemEx* (21), that propagates the Bloch-McConnell equations (22) numerically to minimize the variance between experimental and calculated data, $\chi^2 = \sum_{i=1}^{N} \left(\frac{I_{Calc,i} - I_{Exp,i}}{\sigma_i}\right)^2$, was used to fit different kinetic models to the data and obtain the best fit exchange parameters. Here I_{Exp} is the experimentally measured intensity of a cross-peak in the ^{1}H-^{15}N HSQC spectrum, I_{Calc} is the intensity calculated using the exchange parameters, and σ is the uncertainty in the measured intensities with the summation extending over all the experimental data points. To carry out model selection we used a total of fourteen residues: Thr 13, Lys 26, Lys 28, Arg 29, Asn 33, Glu 37, Lys 41, Met 42, Ile 43, Ser 50, Leu 52, Leu 55, and Lys 59 for which $|\Delta\varpi_{FU}|$ values obtained by a simple two-state analysis were greater than 4 ppm, and Ser 56 which gave a distinct dip at ϖ_{I2}. Rates and populations obtained from fits to this set of residues were used to analyze the CEST profiles from all of the other residues. During the fitting process, initial estimates of ϖ_U were obtained from the minor state dip positions in the CEST profiles while ϖ_{I1} was initialized to the CPMG derived chemical shifts of the folding intermediate of the WT FF domain (23) for

all sites except Gln 38, Gly 39 and Met 40 that are proximal to the site of mutation. For these residues ϖ_{I1} was initialized to different values in separate minimizations with the exchange parameters fixed to obtain the 'best' estimates for ϖ_{I1}. For Ser 56, ϖ_{I2} was initialized to the position of the dip that arises from I2 for this residue, while for the other sites minimization was initialized at various starting positions in the vicinity of ϖ_{I1} to find the 'right' ϖ_{I2}. Once it was established that ϖ_{I2} could be obtained from A17G FF + 20% glycerol, we used these chemical shift values as the initial guesses for ϖ_{I2} except for residues Glu 16, Ala 17, Lys18, Gln 38, Gly 39, and Met 40 that are close to the A17G and A39G sites of mutation; for these residues ϖ_{I2} was initialized to different values with the exchange parameters fixed to obtain the best estimate of ϖ_{I2}. The same procedure was used to initialize ϖ_{I1} and ϖ_{I2} values for the three-state fits of A39G FF CEST profiles recorded in 25% glycerol buffer (Fig. 4E). Fits of the 1M urea (A39G), 10% TFE (A39G) and 20% glycerol (A17G FF) datasets were performed by starting minimization with the minor state chemical shifts set to the positions of the corresponding minor state dips in the CEST profiles. Uncertainties in the best-fit parameters were estimated using the covariance matrix approach or via Monte Carlo/Bootstrap procedures with 200 repeats (24, 25). We did not analyze data recorded from the first 9 residues that are part of the disordered tail.

The kinetic matrix (K) for N state exchange that is intrinsic to the Bloch-McConnell equations (22), and required for the analysis of the dynamics of the system, is related to rates and populations of the states as follows: $K_{i,j} = k_{ji}$ when $i \neq j$ and $K_{i,i} = -\sum_{j=1}^{N} k_{ij}$ $(j \neq i)$. Here $k_{ij} = k_{ex,ij}\frac{p_j}{p_i+p_j}$ is the rate constant for the reaction from state i to j (26, 27). The populations $P(t)$ at any time t after the start of the reaction can be calculated according to $P(t) = e^{Kt}P(0)$, where $P(0)$ and $P(t)$ are column vectors that contain the populations of the different states at time 0 and t, respectively. The relaxation timescale for the i^{th} exchange process is given by $\tau_i = -1/\lambda_i$ where λ_i is an eigenvalue of K. One of the N eigenvalues of K will be 0 and the eigenvector corresponding to this eigenvalue contains the equilibrium populations.

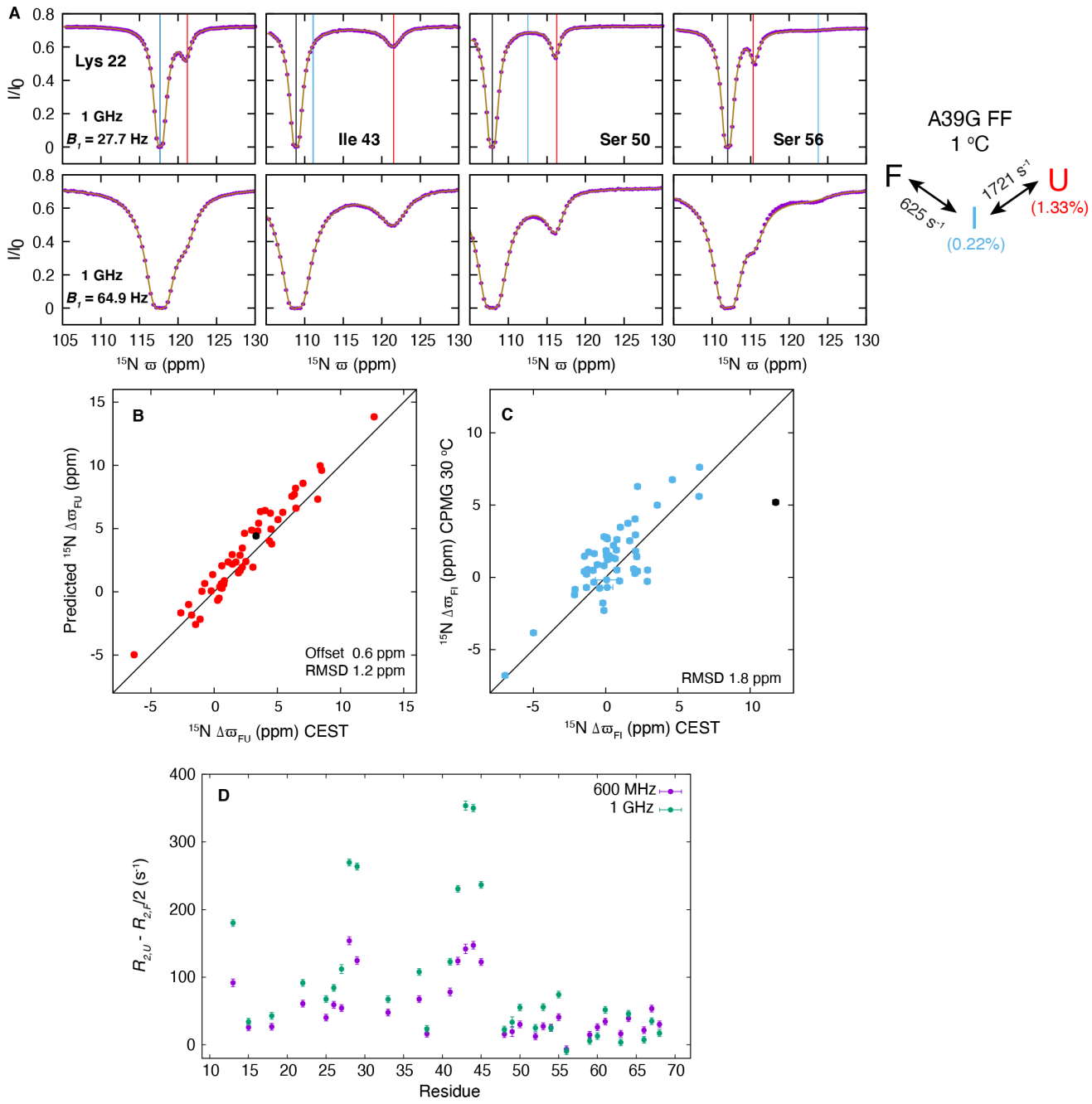

Figure S1 Modelling the folding of A39G FF via a global three-site exchange scheme with an on-pathway intermediate (I). A) ^{15}N CEST profiles (B_1 = 27.7 and 64.9 Hz) for residues Lys 22, Ile 43, Ser 50 and Ser 56 (1 °C, 1 GHz) are shown along with the linear three-state model on the right used to analyze the CEST data. The chemical shifts of the minor states obtained from the three-state analysis are indicated with cyan and red lines for the I and U states, respectively, with the position of the major native state highlighted with a black line. The experimental data points are shown in magenta and the brown line was calculated using the global three-state best fit parameters with R_{2U} allowed to vary from site to site. B) Comparison of $\Delta\varpi_{FU}$ values obtained using the three-state analysis (A) with those predicted using unfolded state chemical shifts calculated with the program POTENCI (28). C) Comparison of $\Delta\varpi_{FI}$ values obtained from the three-state analysis above (A) with those reported at 30 °C for WT FF based on a previous analysis of CPMG data (23). In B and C data from Ser 56 is shown in black and not included in the RMSD and offset calculations as the I state dip arises from a new intermediate (I2) that is not accounted for in the three state model (See text). D) ^{15}N R_{ex} values at 600 MHz and 1 GHz for residues (with $|\Delta\varpi_{FU}| > 2$ ppm) in the U state, approximated as $R_{2,U}$ - $R_{2,F}$/2. R_{ex} values are large, indicating that U exchanges with an additional state beyond I (*i.e.*, the exchange reaction is more complex than three-state).

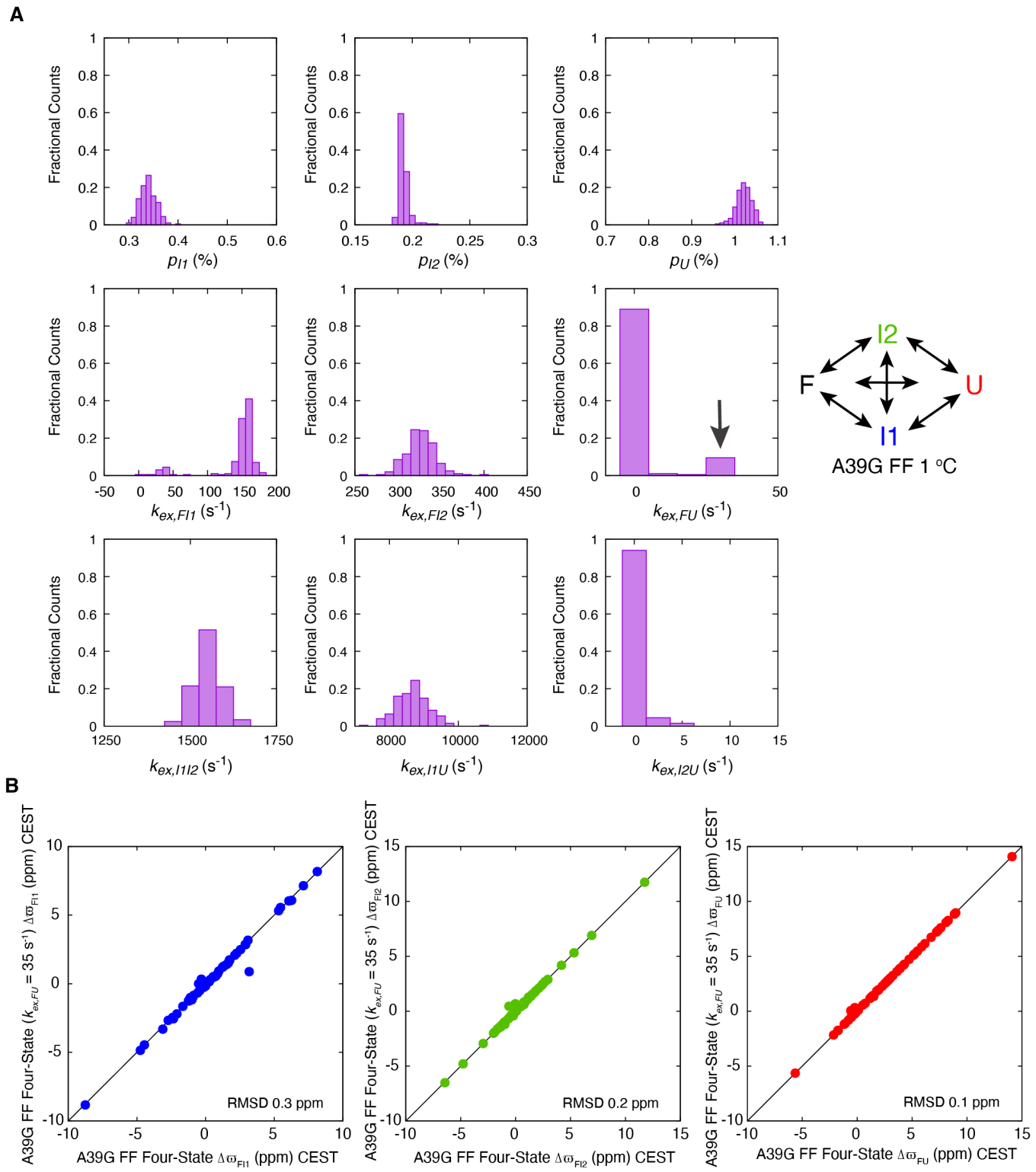

Figure S2 Assessing the robustness of the four-state exchange parameters for the A39G FF domain folding reaction. (A) Distributions of four-state exchange parameters obtained from a 'dropout' analysis. Two hundred synthetic datasets were generated by randomly discarding ~30% of the ^{15}N CEST profiles entirely and the remaining profiles fit to the model shown on the right in which all four-states interconvert with each other. All the populations and most of the exchange rates are well defined. About 90% (10%) of the trials result in $k_{ex,FU}$ ~0 s^{-1} ($k_{ex,FU}$ ~35 s^{-1}), with a concomitant decrease in $k_{ex,FI1}$ from ~160 s^{-1} to ~40 s^{-1} for $k_{ex,FU}$ ~35 s^{-1}. (B) The extracted chemical shifts do not vary between fits with $k_{ex,FU}$ =0 s^{-1} or $k_{ex,FU}$ =35 s^{-1}.

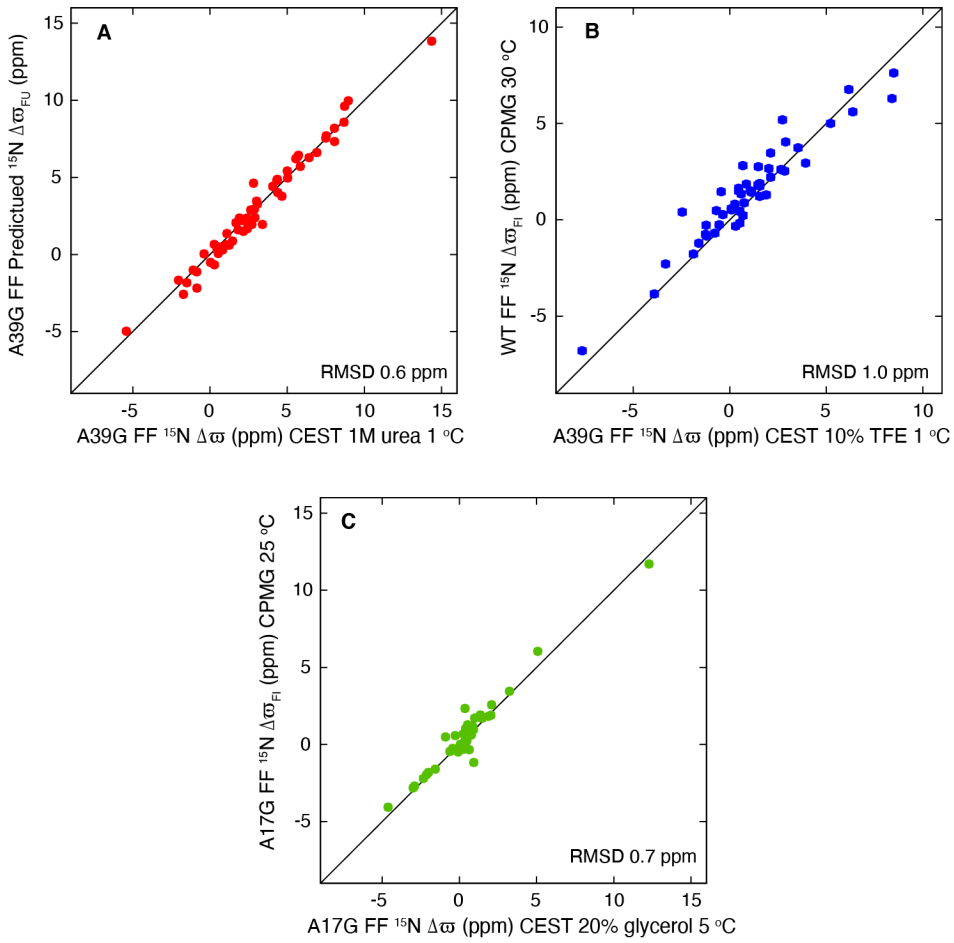

Figure S3 Additives and mutations simplify FF domain dynamics. A) Comparison of $\Delta\varpi_{FU}$ values obtained via a two-state analysis of A39G FF + 1 M urea CEST data (1 °C) with $\Delta\varpi_{FU}$ values obtained using U state shifts predicted by the program POTENCI (28). B) Comparison of $\Delta\varpi$ values generated from a two-state analysis of A39G FF + 10% TFE CEST data (1 °C) with $\Delta\varpi_{FI}$ values obtained from CPMG derived shifts of the folding intermediate of the WT FF domain, 30 °C (8, 23). The good correlation establishes that the minor state populated by A39G FF in the presence of 10% TFE has a structure similar to the folding intermediate of WT FF detected previously at 30 °C. C) Comparison of $\Delta\varpi$ values fitted using a two-state analysis of A17G FF CEST data recorded in the presence of 20% glycerol, 5 °C with $\Delta\varpi_{FI}$ values obtained using CPMG derived chemical shifts of the folding intermediate of A17G FF at 25 °C (8). The excellent correlation establishes that the minor state detected for A17G FF at 5 °C, 20% glycerol, is structurally very similar to the folding intermediate detected earlier (8).

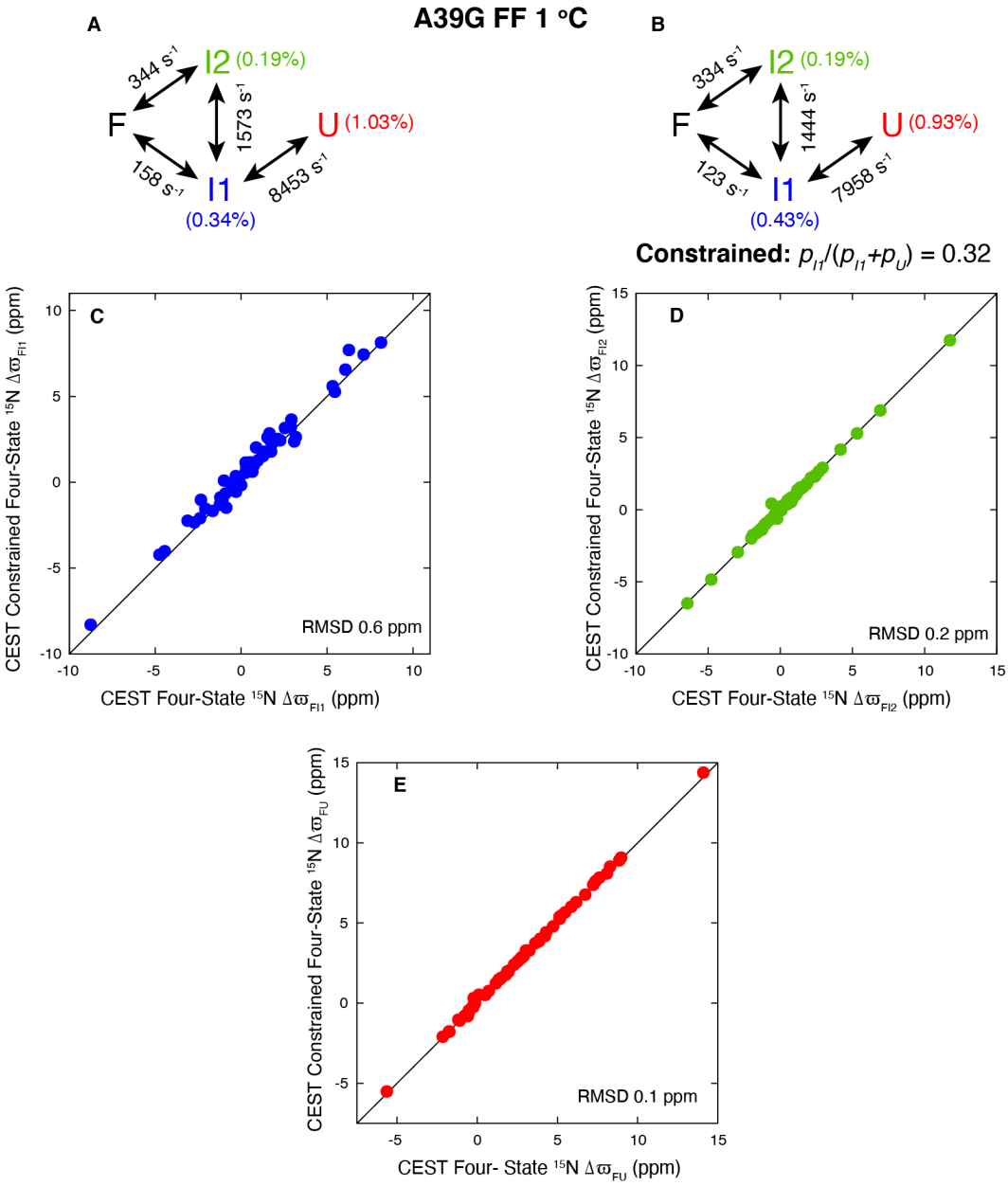

Figure S4 Four-state fits of the A39G FF ^{15}N CEST data, either unconstrained or constrained such that $p_{I1}/(p_{I1} + p_U)$ = 0.32, give similar extracted parameters, as indicated in A and B. In both models $p_U > p_{I1} > p_{I2}$ and the chemical shifts of the minor states are essentially identical (C-E).

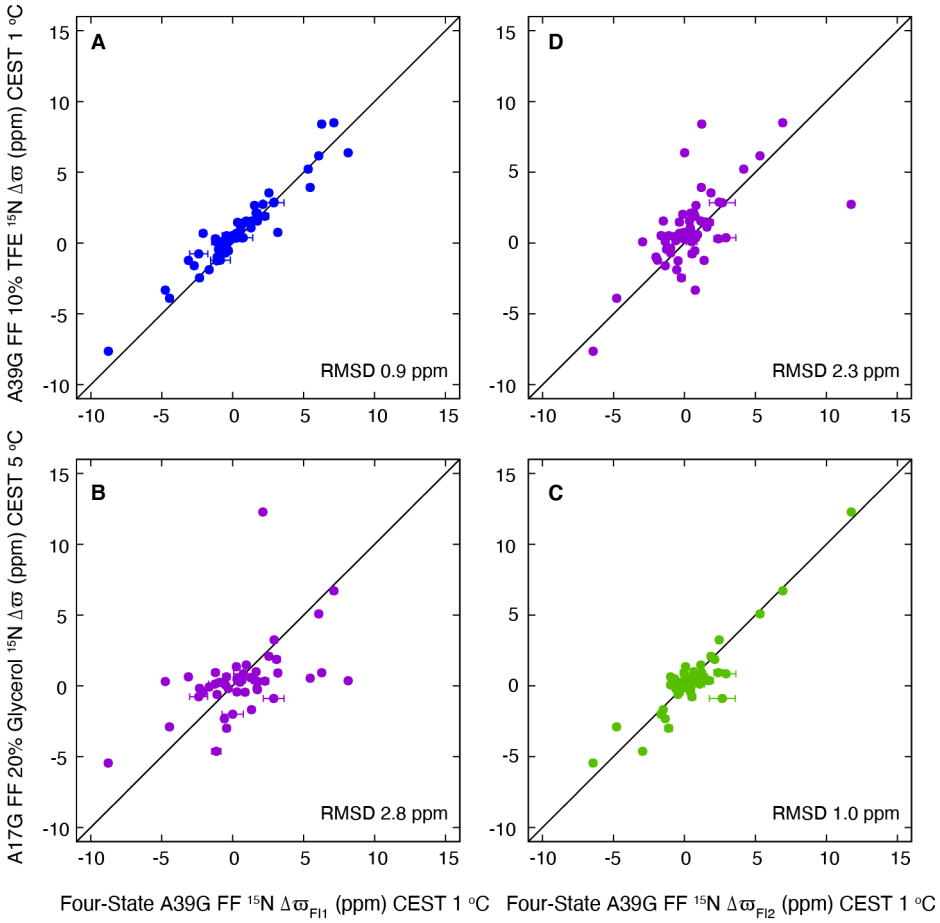

Figure S5 Intermediates I1 and I2 can be readily distinguished from each other based on CEST data. (A,B) Comparison of $\Delta\varpi_{FI1}$ values from the four-state analysis with the two-state ^{15}N $\Delta\varpi$ values obtained for A39G FF + 10% TFE (A) and for A17G FF + 20% glycerol (B). (C,D) Comparison of $\Delta\varpi_{FI2}$ values from the four-state analysis with the two-state ^{15}N $\Delta\varpi$ values obtained for A17G + 20% glycerol (C) and for A39G FF + 10% TFE (D). Data plotted in panels A and C are also plotted in the main text figures, 4G and 4H respectively.

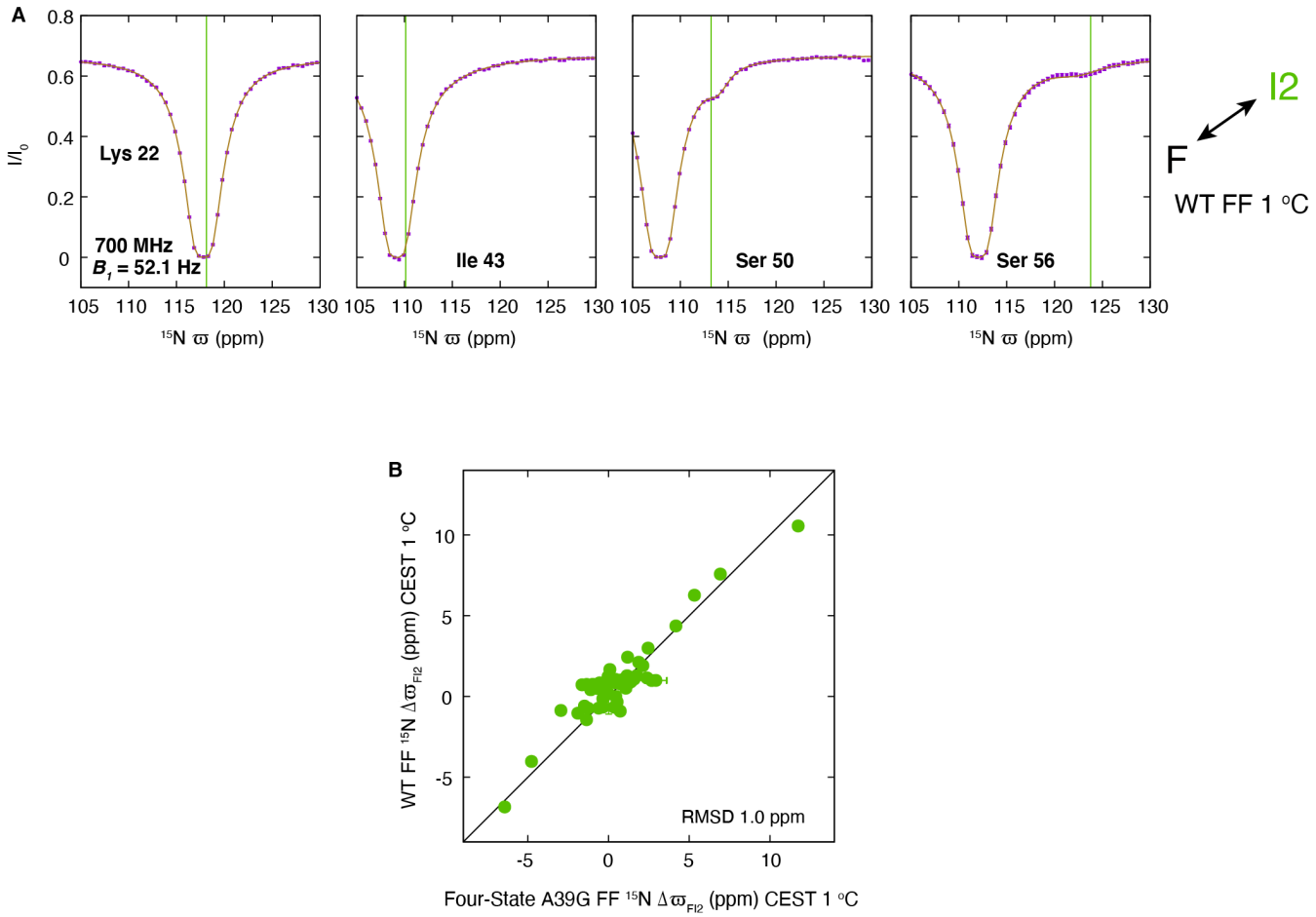

Figure S6 The WT FF domain populates the I2 state. A) ^{15}N CEST profiles for Lys 22, Ile 43, Ser 50 and Ser 56 from WT FF (*SI Appendix* Table S1: Sample 6, 1 °C) recorded at 700 MHz with B_1 = 52.1 Hz. The ϖ_{I2} shifts obtained from the four-state analysis of the A39G FF CEST data (Fig. 4, *SI Appendix*, Table S4) are shown using the green vertical lines. Minor state dips can be clearly seen at the predicted positions for Ser 50 and Ser 56. The experimental CEST points are in magenta and best fit curves in brown, generated from the global optimized exchange parameters ($k_{ex,FI2}$ = 354 s^{-1}, p_{I2} = 0.19%) with $R_{2,I2}$ unconstrained. B) Linear correlation plot of four-state and two-state $\Delta\varpi_{FI2}$ values obtained from the analysis of A39G FF and WT FF CEST profiles, respectively, confirming that WT FF samples the I2 state. Previous CPMG-based studies at 30 °C established that the folding of WT FF proceeds via an intermediate (8, 23) whose chemical shifts are similar to I1 (see text, *SI Appendix* Fig. S3B). Thus, given that the WT FF domain populates the I2 state, its folding can also be described in terms of a four-state equilibrium. At 1 °C the populations of both the I1 and U states have decreased considerably so that reasonable fits can be achieved with a two-state model. As the dips at ϖ_{I2} are broadened, presumably because FF WT samples I1 in addition to I2, $R_{2,I2}$ was allowed to float during the two-state fits for sites where a clear minor state dip was seen (Ser 50, Leu 52, Ala 53, Leu 55, Ser 56, and Lys 59).

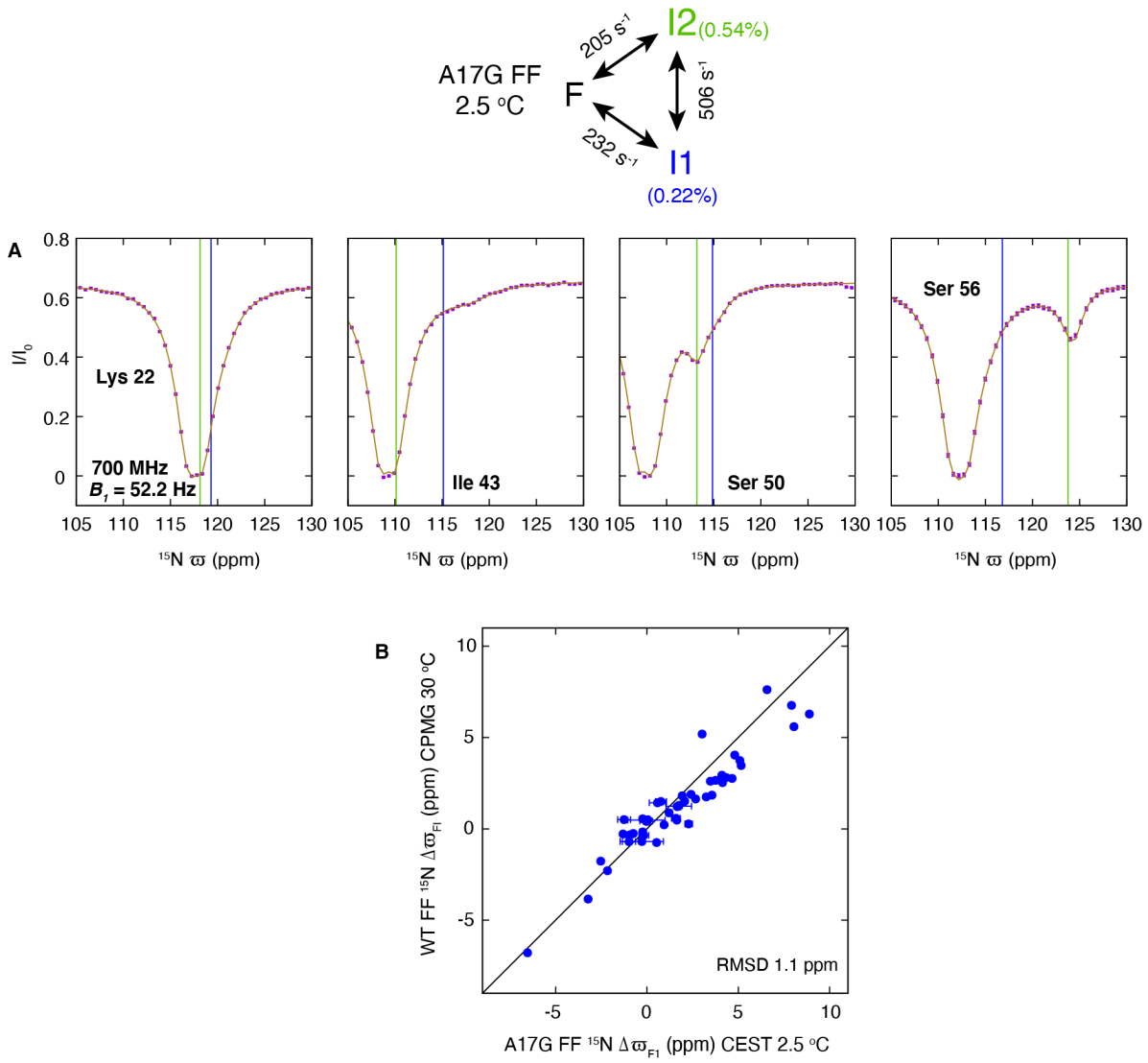

Figure S7 The A17G FF domain populates the I1 state. A) ^{15}N CEST profiles for Lys 22, Ile 43, Ser 50 and Ser 56 of A17G FF (*SI Appendix* Table S1: Sample 7, 2.5 °C) recorded at 700 MHz with B_1 = 52.2 Hz. The ϖ_{I2} shifts obtained from the four-state analysis of A39G FF CEST profiles (Fig. 4) are highlighted by green vertical lines and WT FF ϖ_I shifts obtained from a previous CPMG study, 30 °C, (23) are indicated using blue vertical lines. The experimental data (magenta) is fit with the model shown on the top, to generate the parameters as indicated. It is worth noting that a two-state model did not fit the CEST data adequately (χ^2_{red} ~1.47) while the three-state model shown above did (χ^2_{red} ~0.45). Thus, the A17G has at least two intermediate states, I1 and I2, as described in the text. At the outset of the fitting process ϖ_{I1} values were initialized to the CPMG derived chemical shifts of the folding intermediate of WT FF (23) and ϖ_{I2} values were set to those obtained from analysis of CEST profiles from A17G FF + 20% glycerol 5 °C (Sample 5, *SI Appendix* Table S1, Table S7). To account for residual U state, $R_{2,I1}$ was floated while $R_{2,I2} = R_{2,F}$ during the fits. B) The strong correlation between the WT FF $\Delta\varpi_{FI}$ values obtained via a previous analysis of CPMG data (30 °C) (23) and the corresponding values from the three-state analysis of the CEST data recorded on A17G FF, 2.5 °C, described here, confirms that A17G FF also samples the I1 state. As A17G FF was shown to populate I2 in a previous study (8), it is clear that folding of A17G FF is also best described in terms of a four-state model, as for A39G and WT FF domains.

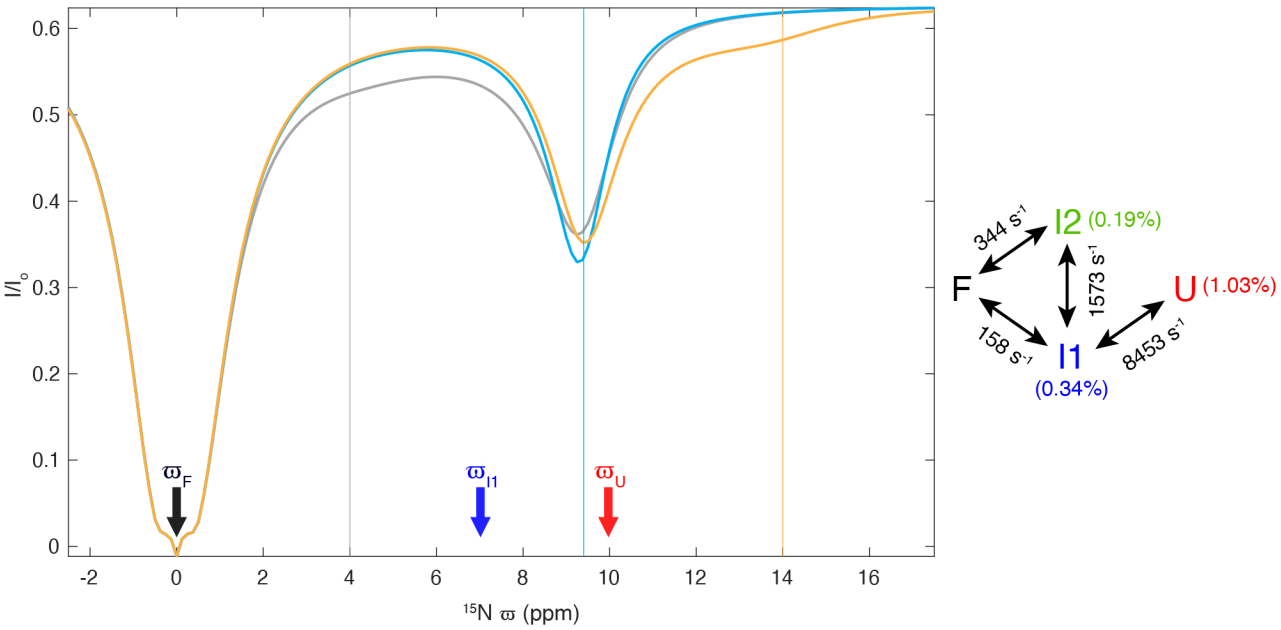

Figure S8 Four-state ^{15}N CEST profiles can be sensitive to resonance frequencies of nuclei in states that cannot be observed. ^{15}N CEST profiles were calculated at a static magnetic field of 1 GHz, B_1 = 50 Hz, T_{EX} = 0.45 s, with the exchange rates and populations set to the best fit values for the A39G FF domain folding reaction obtained via fits to experimental data . ϖ_F, ϖ_{I1} and ϖ_U were set to 0, 7 and 10 ppm, respectively, as indicated by the arrows. Profiles calculated with ϖ_{I2} = 4, 9.4 and 14 ppm are shown in grey, cyan and orange, respectively, indicated by vertical lines. When ϖ_{I2} = 4 ppm (grey) there is a loss of intensity in the 4 - 7 ppm range, and when ϖ_{I2} = 14 ppm (similar to the downfield shift observed for Ser 56 of A39G FF) there is clear broad dip due to I2 near 14 ppm. When ϖ_{I2} = 9.4 ppm the averaged minor state dip that results from the rapid exchange between I1 and U is narrowed, as its position at 9.3 ppm is close to ϖ_{I2} = 9.4 ppm, and thus exchange broadening between U+I1 and I2 is reduced. It is clear that shapes of CEST profiles depend on both the kinetics of the involved processes and the chemical shifts of the different states such that in at least some cases detailed information about conformers that are ‘CEST-invisible’ can be obtained.

Sample	Protein	Buffer	Temperature °C	^{15}N CEST NMR Experiments						Comments
				B_0 (MHz)	B_1 (Hz)	T_{EX} (ms)	Center [ϖ_{cent}] (ppm)	Range (Hz)	Step Size (Hz)	
1	A39G FF	50 mM sodium acetate, 100 mM NaCl, 2mM EDTA, 2mM NaN_3, 2.5% D_2O (pH 5.7)	1	1000	8.3	500	118.318	±1175	10	^{15}N CEST data at 600 MHz & 1 GHz were used for the bulk of the analysis. D_2O concentration was minimized to reduce artifacts resulting from H/D exchange.
					27.7	450	118.318	±1292.5	27.5	
					64.9	450	118.318	±1537.5	37.5	
					159.6	370	118.318	±1640.0	40	
					224.5	350	118.318	±2035	55	
				600	15.9	500	118.318	±900	15	
					29.1	450	118.318	±900	18	
2	A39G FF	50 mM sodium acetate, 100 mM NaCl, 2mM EDTA, 2mM NaN_3, 25% glycerol, 10% D_2O (pH 5.7)	15	700	18.3	500	117.928	±1086.5	20.5	^{15}N CEST data at 700 MHz used for three-state fits between F, I1 and I2 (Fig. 4E).
					31.3	475	117.928	±1260	30	
					52.2	450	117.928	±1400	35	
					114.8	350	117.928	±1660	41.5	
					219.2	350	117.928	±1746	48.5	
3	A39G FF	50 mM sodium acetate, 100 mM NaCl, 2mM EDTA, 2mM NaN_3, 1M urea, 10% D_2O (pH 5.7)	1	700	18.3	500	117.821	±1086.5	20.5	^{15}N CEST data at 700 MHz used to obtain U state shifts via two-state analysis (Fig. 4B).
					33.9	475	117.821	±1260	30	
4	A39G FF	50 mM sodium acetate, 100 mM NaCl, 2mM EDTA, 2mM NaN_3, 10% TFE, 10% D_2O (pH 5.7)	1	700	10.4	500	117.821	±1075	12.5	^{15}N CEST data at 700 MHz used to obtain I1 state shifts via two-state analysis (Fig. 4C).
					18.2	500	117.821	±1086.5	20.5	
5	A17G FF	50 mM sodium acetate, 100 mM NaCl, 2mM EDTA, 2mM NaN_3, 20% glycerol, 10% D_2O (pH 5.7)	5	700	10.3	500	117.822	±900	15	^{15}N CEST data at 700 MHz used to obtain I2 state shifts via two-state analysis (Fig. 4D).
					25.8	500	117.822	±1100	25	
6	WT FF	50 mM sodium acetate, 100 mM NaCl, 2mM EDTA, 2mM NaN_3, 10% D_2O (pH 5.7)	1	700	26.0	500	117.825	±1100	25	^{15}N CEST data at 700 MHz showing that WT FF populates I2 (Fig. S6) in addition to I1.
					52.1	450	117.825	±1400	35	
					114.6	350	117.825	±1746	48.5	
7	A17G FF	50 mM sodium acetate, 100 mM NaCl, 2mM EDTA, 2mM NaN_3, 10% D_2O (pH 5.7)	2.5	700	18.3	500	117.811	±1260	20	^{15}N CEST data at 500 and 700 MHz used to obtain I1 state shifts of A17G FF via three-state (F, I1 & I2) analysis (Fig. S7), thereby establishing that A17G FF populates I1 in addition to I2.
					52.2	450	117.811	±1400	40	
					104.4	350	117.811	±1746	48.5	
					208.8	350	117.811	±1746	48.5	
				500	51.8	450	119.811	±1250	50	

Table S1 Details of the different samples and ^{15}N CEST experiments used in this study. Seven samples in total were used. The FF variant, buffer composition, temperature, spectrometer frequency (B_0), ^{15}N B_1 field applied during the T_{EX} period, and the length of the T_{EX} period are listed. ^{15}N CEST profiles were recorded by weak B_1 irradiation at offsets ranging from ϖ_{cent} – Range to ϖ_{cent} + Range in steps of 'step size' resulting in a total of [(2×Range)/(step size) + 2] planes that includes the reference plane recorded with T_{EX} = 0. All experiments were carried using the regular ^{15}N CEST pulse scheme (1) in which ^{1}H decoupling is performed using $90_x240_y90_x$ composite pulses (13) during the T_{EX} period.

	Model		Residues	^{15}N CEST Datasets B_0 (MHz) B_1 (Hz)	Constraints	χ^2_{red}	Comments
	States	Description					
1	2	F ↔ U	Set 1	Set 1	$R_{2U} = R_{2F}/2$	5.29	
2	2	F ↔ U	Set 1	Set 1	None	1.43	R_{2U} unconstrained.
3	3	F ↔ I1 ↔ U	Set 1	Set 2	$R_{2I1} = R_{2F}$ $R_{2U} = R_{2F}/2$	2.44	
4	3	F ↔ I1 ↔ U	Set 1	Set 2	$R_{2I1} = R_{2F}$	1.27	R_{2U} unconstrained.
5	3	Triangular	Set 1	Set 2	$R_{2I1} = R_{2F}$ $R_{2U} = R_{2F}/2$	2.44	
6	3	Triangular	Set 1	Set 2	$R_{2I1} = R_{2F}$	1.0	R_{2U} unconstrained.
7	4	F ↔ I2 ↔ I1 ↔ U	Set 1	Set 2	$R_{2I1} = R_{2I2} = R_{2F}$ $R_{2U} = R_{2F}/2$	1.1	
9	4	I2 ↔ F ↔ I1 ↔ U	Set 1	Set 2	$R_{2I1} = R_{2I2} = R_{2F}$ $R_{2U} = R_{2F}/2$	1.63	
10	4	All 4 states exchange with each other	Set 1	Set 2	$R_{2I1} = R_{2I2} = R_{2F}$ $R_{2U} = R_{2F}/2$	0.9	
11	4	$k_{ex,I2U} = k_{ex,FU} = 0$ s^{-1}	Set 1	Set 2	$R_{2I1} = R_{2I2} = R_{2F}$ $R_{2U} = R_{2F}/2$	0.9	
12	4	$k_{ex,I2U} = k_{ex,FU} = 0$ s^{-1}	Set 1	Set 2	$R_{2I1} = R_{2I2} = R_{2F}$	0.86	R_{2U} unconstrained.
13	4	$k_{ex,I2U} = k_{ex,FU} = 0$ s^{-1}	Set 1	Set 2	$R_{2I1} = R_{2I2} = R_{2F}$ $R_{2U} = R_{2F}/2$ $p_{I1}/(p_{I1} + p_U) = 0.32$	0.91	$p_{I1}/(p_{I1} + p_U) = 0.32$
14	3	Triangular	Set 2	Set 2	$R_{2I1} = R_{2F}$ $R_{2U} = R_{2F}/2$	1.67	
15	3	Triangular	Set 2	Set 2	$R_{2I1} = R_{2F}$	1.01	R_{2U} unconstrained.
16	4	F ↔ I2 ↔ I1 ↔ U	Set 2	Set 2	$R_{2I1} = R_{2I2} = R_{2F}$ $R_{2U} = R_{2F}/2$	0.93	
17	4	I2 ↔ F ↔ I1 ↔ U	Set 2	Set 2	$R_{2I1} = R_{2I2} = R_{2F}$ $R_{2U} = R_{2F}/2$	1.47	

Table S2 Summary of various exchange models fitted to A39G FF ^{15}N CEST profiles recorded at 600 MHz and 1 GHz. Sample and experimental details are presented in *SI Appendix* Table S1, Sample 1. Set 1 under 'Residues' refers to ^{15}N CEST profiles from Thr 13, Lys 26, Lys 28, Arg 29, Asn 33, Glu 37, Lys 41, Met 42, Ile 43, Ser 50, Leu 52, Leu 55, Ser 56 and Lys 59; Set 2 refers to all the residues in Set 1 except for Ser 56. Set 1 under ^{15}N datasets refers to ^{15}N CEST profiles recorded with B_1 = 8.3 and 27.7 Hz at 1 GHz and 15.9 and 29.1 Hz at 600 MHz while Set 2 contains ^{15}N CEST profiles with B_1 = 64.9, 159.6, and 224.5 Hz at 1 GHz in addition to the ones in Set 1.

	Model		Residues	^{15}N CEST Datasets B_0 (MHz) B_1 (Hz)	Constraints	χ^2_{red}	Comments
	States	Description					
1	3	F ↔ I2 ↔ I1	Set 1	Set 1	$R_{2I1} = R_{2I2} = R_{2F}$	1.22	
2	3	F ↔ I1 ↔ I2	Set 1	Set 1	$R_{2I1} = R_{2I2} = R_{2F}$	1.40	
3	3	I2 ↔ F ↔ I1	Set 1	Set 1	$R_{2I1} = R_{2I2} = R_{2F}$	3.3	
4	3	Triangular	Set 1	Set 1	$R_{2I1} = R_{2I2} = R_{2F}$	1.05	
5	3	Triangular	Set 1	Set 1	$R_{2I2} = R_{2F}$	0.98	R_{2I1} unconstrained.

Table S3 Summary of various exchange models fitted to A39G FF+25% glycerol ^{15}N CEST profiles recorded at 700 MHz (15 ^{o}C; see Fig. 4E). Sample and experimental details are presented in *SI Appendix* Table S1, Sample 2. Set 1 under residues refers to ^{15}N CEST profiles from Thr 13, Lys 26, Lys 28, Arg 29, Asn 33, Glu 37, Lys 41, Met 42, Ile 43, Ser 50, Leu 52, Leu 55, Ser 56, and Lys 59. Set 1 under ^{15}N CEST datasets refers to ^{15}N CEST profiles recorded with B_1 = 18.3, 31.3, 52.2, 114.8, and 219.2 Hz at 700 MHz.

Residue		ϖ_F	$\Delta\varpi_{FI1}$ (ppm)		$\Delta\varpi_{FI2}$ (ppm)		$\Delta\varpi_{FU}$ (ppm)	
			Value	Uncertainty	Value	Uncertainty	Value	Uncertainty
10	T	114.456	0.74	0.67	2.93	0.69	1.78	0.23
12	N	119.937	-0.00	0.74	-1.65	0.23	-0.33	0.27
13	T	108.200	0.26	0.20	0.08	0.20	5.49	0.20
14	K	123.087	-2.39	0.63	0.53	0.26	-0.23	0.20
15	E	119.161	0.30	0.20	0.42	0.20	2.51	0.20
16	E	119.979	-0.13	0.20	0.02	0.20	1.88	0.20
17	A	125.114	-2.72	0.21	-1.36	0.20	-0.53	0.20
18	K	117.296	0.33	0.20	0.91	0.20	2.76	0.20
19	Q	119.029	-0.51	0.20	-0.98	0.20	1.51	0.20
20	A	122.950	-0.44	0.25	-0.98	0.20	1.17	0.20
21	F	119.052	-1.21	0.24	2.39	0.32	0.72	0.21
22	K	117.676	0.52	0.20	0.44	0.20	4.29	0.20
23	E	120.495	-0.87	0.69	-1.90	0.20	0.10	0.24
24	L	123.032	-1.24	0.46	1.07	0.34	-0.13	0.20
25	L	118.123	0.30	0.20	-0.70	0.20	3.62	0.20
26	K	115.728	2.55	0.20	1.87	0.20	6.17	0.20
27	E	122.812	-4.75	0.20	0.76	0.20	-1.18	0.20
28	K	113.887	1.65	0.20	0.65	0.20	8.29	0.20
29	R	115.358	0.87	0.20	-0.36	0.24	7.38	0.20
30	V	120.652	-3.12	0.20	1.38	0.20	3.03	0.20
32	S	116.036	-2.09	0.22	-0.35	0.22	1.35	0.20
33	N	115.649	1.76	0.20	-0.12	0.20	5.16	0.20
34	A	123.221	-0.92	0.25	0.51	0.37	1.31	0.20
35	S	117.076	-0.31	0.20	0.72	0.20	-1.73	0.20
36	W	123.210	3.18	0.20	-0.03	0.27	-0.59	0.21
37	E	116.191	1.72	0.20	0.45	0.20	5.87	0.20
38	Q	117.242	1.23	0.20	1.50	0.20	2.91	0.20
39	G	107.524	0.25	0.20	-0.43	0.20	1.97	0.20
40	M	120.731	-1.10	0.20	-2.01	0.20	-0.80	0.20
41	K	114.658	2.92	0.20	2.45	0.20	7.23	0.20
42	M	113.557	1.54	0.20	0.81	0.20	7.62	0.20
43	I	108.880	6.27	0.20	1.22	0.20	14.10	0.20
44	I	119.108	-2.34	0.20	-0.21	0.25	5.12	0.20
45	N	116.638	-1.00	0.20	-1.27	0.20	5.23	0.20
46	D	123.175	3.09	0.25	2.13	0.20	-0.54	0.20
48	R	116.224	0.96	0.20	1.15	0.20	2.79	0.20
50	S	107.883	6.07	0.20	5.32	0.20	8.98	0.20
51	A	123.559	-0.58	0.20	-1.36	0.20	2.29	0.20
52	L	111.376	7.13	0.20	6.93	0.20	8.86	0.20
53	A	126.420	-4.45	0.20	-4.78	0.20	-2.15	0.20
54	K	115.773	1.33	0.20	-1.49	0.20	3.93	0.20
55	L	128.324	-8.76	0.20	-6.44	0.20	-5.64	0.20
56	S	112.024	2.13	0.20	11.75	0.20	3.85	0.20
57	E	122.123	-1.15	0.33	-2.95	0.20	-0.25	0.20
58	K	121.331	-0.43	0.23	-1.11	0.26	1.43	0.20
59	K	116.410	5.32	0.20	4.18	0.20	6.74	0.20
60	Q	119.261	1.29	0.20	0.40	0.20	2.83	0.20
61	A	123.081	0.57	0.20	1.58	0.20	2.80	0.20
62	F	121.188	-1.10	0.20	-0.46	0.20	-1.10	0.20
63	N	118.239	2.27	0.26	0.74	0.21	3.25	0.20
64	A	122.397	0.34	0.20	1.75	0.28	2.64	0.20
65	Y	120.747	-1.66	0.20	-0.55	0.20	-1.76	0.20
66	K	119.379	2.89	0.73	2.67	0.91	4.73	0.24
67	V	114.492	8.14	0.20	0.01	0.20	8.09	0.20
68	Q	120.614	5.46	0.20	1.18	0.20	4.22	0.20
69	T	114.420	1.74	0.20	0.35	0.20	1.93	0.20
70	E	123.573	0.65	0.24	0.78	0.20	0.51	0.20
71	K	127.565	-0.31	0.20	-0.61	0.20	-0.22	0.20

Table S4 Chemical shifts of the F, I1, I2 and U states of A39G FF, 1 ^{o}C, obtained from the four-state analysis ($k_{ex,FI1}$ = 158 $\pm$ 20 s^{-1}, $k_{ex,FI2}$ = 344 $\pm$ 20 s^{-1}, $k_{ex,I1I2}$ = 1573 $\pm$ 50 s^{-1}, and $k_{ex,I1U}$ = 8453 $\pm$ 400 s^{-1}, and fractional populations p_{I1}= 0.34 $\pm$ 0.05 %, p_{I2} = 0.19 $\pm$ 0.01 % and p_U = 1.03 $\pm$ 0.05 %) of ^{15}N CEST data recorded at 600 MHz and 1 GHz (Sample 1, *SI Appendix* Table S1). The minimum uncertainty in $\Delta\varpi$ is set to 0.2 ppm.

Residue		ϖ_F	$\Delta\varpi_{FU}$ (ppm)	
			Value	Uncertainty
10	T	114.659	1.82	0.20
12	N	120.133	0.48	0.20
13	T	108.175	5.56	0.20
14	K	123.202	0.28	0.20
15	E	119.130	2.64	0.20
16	E	119.899	2.15	0.20
17	A	125.064	-0.38	0.20
18	K	117.327	3.02	0.20
19	Q	119.031	1.91	0.20
20	A	122.953	1.68	0.20
21	F	119.037	0.82	0.20
22	K	117.652	5.01	0.20
23	E	120.499	1.09	0.20
24	L	123.032	0.53	0.20
25	L	118.096	4.37	0.20
26	K	115.725	6.42	0.20
27	E	122.767	-1.09	0.20
28	K	113.887	8.68	0.20
29	R	115.469	7.50	0.20
30	V	120.589	2.88	0.20
32	S	116.113	0.47	0.20
33	N	115.700	5.03	0.20
34	A	123.084	1.24	0.20
35	S	117.149	-1.72	0.20
36	W	123.226	0.04	0.20
37	E	116.237	5.85	0.20
38	Q	117.217	3.07	0.20
39	G	107.484	2.21	0.20
40	M	120.715	-0.86	0.20
41	K	114.714	7.53	0.20
42	M	113.586	8.06	0.20
43	I	108.873	14.36	0.20
44	I	119.149	5.67	0.20
45	N	116.665	5.73	0.20
46	D	123.172	0.29	0.20
48	R	116.184	2.83	0.20
50	S	107.911	8.96	0.20
51	A	123.578	2.37	0.20
52	L	111.472	8.72	0.20
53	A	126.422	-2.04	0.20
54	K	115.736	4.33	0.20
55	L	128.356	-5.42	0.20
56	S	112.100	4.06	0.20
57	E	122.081	1.06	0.20
58	K	121.366	1.46	0.20
59	K	116.444	6.92	0.20
60	Q	119.336	2.91	0.20
61	A	123.084	2.71	0.20
62	F	121.181	-0.84	0.20
63	N	118.237	3.40	0.20
64	A	122.420	2.42	0.20
65	Y	120.679	-1.50	0.20
66	K	119.555	4.38	0.20
67	V	114.780	8.07	0.20
68	Q	120.630	4.66	0.20
69	T	114.308	2.17	0.20
70	E	123.540	0.58	0.20
71	K	127.606	-0.21	0.20

Table S5 Chemical shifts of the F and U states of A39G FF + 1 M urea, 1 °C, obtained from the two-state analysis ($k_{ex,FU}$ = 17.9 ± 2 s^{-1}, p_U = 7.4 ± 0.4%) of 700 MHz ^{15}N CEST data (Sample 3, *SI Appendix* Table S1). The minimum uncertainty in $\Delta\varpi$ is set to 0.2 ppm.

Residue		ϖ_F	$\Delta\varpi_{FI1}$ (ppm)	
			Value	Uncertainty
10	T	114.270	0.38	0.20
12	N	119.239	0.52	0.20
13	T	108.196	0.68	0.20
14	K	122.883	-0.77	0.20
15	E	118.921	0.46	0.20
16	E	119.951	0.26	0.20
17	A	124.990	-1.60	0.20
18	K	117.123	0.59	0.20
19	Q	118.855	-0.70	0.20
20	A	122.843	-0.36	0.20
21	F	118.931	0.30	0.20
22	K	117.632	0.86	0.20
23	E	120.046	-1.21	0.20
25	L	118.185	0.46	0.20
26	K	115.871	3.54	0.20
27	E	122.682	-3.32	0.20
28	K	113.928	2.11	0.20
29	R	115.270	1.48	0.20
30	V	120.345	-1.22	0.20
32	S	115.611	0.69	0.20
33	N	115.366	2.02	0.20
34	A	123.136	0.09	0.20
35	S	117.341	-0.55	0.20
36	W	123.080	0.75	0.20
37	E	116.195	2.12	0.20
38	Q	116.999	1.49	0.20
39	G	107.146	0.35	0.20
40	M	120.444	-1.00	0.20
41	K	114.869	2.89	0.20
42	M	113.575	2.65	0.20
43	I	108.881	8.40	0.20
44	I	119.080	-2.46	0.20
45	N	116.607	-0.44	0.20
48	R	116.206	1.55	0.20
50	S	107.971	6.16	0.20
51	A	123.587	0.11	0.20
52	L	111.162	8.50	0.20
53	A	126.363	-3.91	0.20
54	K	115.715	1.56	0.20
55	L	128.151	-7.65	0.20
56	S	111.938	2.73	0.20
57	E	121.925	0.08	0.20
58	K	120.820	0.52	0.20
59	K	116.351	5.22	0.20
60	Q	119.338	1.07	0.20
61	A	123.086	1.13	0.20
62	F	120.856	-1.26	0.20
63	N	118.189	1.89	0.20
64	A	122.234	1.46	0.20
65	Y	120.567	-1.88	0.20
66	K	119.730	2.85	0.20
67	V	114.850	6.38	0.20
68	Q	119.877	3.93	0.20
69	T	113.494	1.55	0.20
70	E	123.336	0.36	0.20
71	K	127.330	0.17	0.20

Table S6 Chemical shifts of the F and I1 states of A39G FF in the presence of 10% TFE, 1 °C, obtained from the two-state analysis ($k_{ex,FI1} = 95.5 \pm 4$ s^{-1}, $p_{I1} = 8.6 \pm 0.1$%) of 700 MHz ^{15}N CEST data (Sample 4, *SI Appendix* Table S1). The minimum uncertainty in $\Delta\varpi$ is set to 0.2 ppm.

Residue		ϖ_F	$\Delta\varpi_{FI2}$ (ppm)	
			Value	Uncertainty
10	T	114.422	0.85	0.20
11	W	121.946	-1.56	0.20
12	N	119.907	-2.00	0.20
13	T	108.600	1.35	0.20
14	K	123.204	-0.76	0.20
15	E	119.286	-0.43	0.20
16	E	119.752	0.77	0.20
17	G	109.890	-0.37	0.20
19	Q	118.487	0.07	0.20
20	A	122.632	0.64	0.20
21	F	119.206	0.94	0.20
22	K	117.521	0.26	0.20
24	L	122.913	0.13	0.20
25	L	117.791	0.49	0.20
26	K	115.516	2.09	0.20
27	E	122.809	0.30	0.20
28	K	113.863	0.99	0.20
29	R	115.297	-0.45	0.20
30	V	120.290	0.64	0.20
32	S	116.027	-0.43	0.20
33	N	115.291	0.30	0.20
34	A	122.714	0.25	0.20
36	W	122.587	0.91	0.20
37	E	116.097	-0.19	0.20
38	Q	117.866	2.04	0.20
39	A	122.238	0.39	0.20
40	M	116.485	-2.13	0.20
41	K	114.200	3.25	0.20
42	M	113.920	0.40	0.20
43	I	109.080	0.93	0.20
44	I	119.410	-0.17	0.20
46	D	123.222	1.87	0.20
48	R	115.902	1.48	0.20
50	S	107.951	5.08	0.20
51	A	123.425	-2.33	0.20
52	L	111.912	6.71	0.20
53	A	125.667	-2.90	0.20
54	K	115.388	-1.68	0.20
55	L	127.976	-5.45	0.20
56	S	112.252	12.28	0.20
57	E	121.743	-4.62	0.20
58	K	121.638	-2.99	0.20
60	Q	119.133	0.57	0.20
61	A	123.154	0.39	0.20
62	F	120.272	-0.61	0.20
63	N	119.134	0.33	0.20
64	A	121.915	0.37	0.20
65	Y	121.060	-0.08	0.20
66	K	119.435	-0.90	0.20
67	V	114.192	0.36	0.20
68	Q	120.212	0.54	0.20
69	T	113.929	-0.27	0.20
70	E	123.159	0.41	0.20
71	K	127.170	-0.20	0.20

Table S7 Chemical shifts of the F and I2 states of A17G FF + 20% glycerol, 5 ^{o}C, obtained from the two-state ($k_{ex,FI2}$ = 104.6 $\pm$ 10 s^{-1}, p_{I2} = 1.0 $\pm$ 0.1%) analysis of 700 MHz ^{15}N CEST data (Sample 5, *SI Appendix* Table S1). The minimum uncertainty in $\Delta\varpi$ is set to 0.2 ppm.

References

1. P. Vallurupalli, G. Bouvignies, L. E. Kay, Studying "invisible" excited protein States in slow exchange with a major state conformation. *J Am Chem Soc* **134**, 8148-8161 (2012).
2. K. M. Ward, A. H. Aletras, R. S. Balaban, A new class of contrast agents for MRI based on proton chemical exchange dependent saturation transfer (CEST). *J Magn Reson* **143**, 79-87 (2000).
3. P. Vallurupalli, A. Sekhar, T. Yuwen, L. E. Kay, Probing conformational dynamics in biomolecules via chemical exchange saturation transfer: a primer. *J Biomol NMR* **67**, 243-271 (2017).
4. S. Forsen, R. A. Hoffman, Study of Moderately Rapid Chemical Exchange Reactions by Means of Nuclear Magnetic Double Resonance. *J Chem Phys* **39**, 2892-2901 (1963).
5. P. C. M. van Zijl, N. N. Yadav, Chemical Exchange Saturation Transfer (CEST): What is in a Name and What Isn't? *Magn Reson Med* **65**, 927-948 (2011).
6. A. Rangadurai, H. Shi, H. M. Al-Hashimi, Extending the Sensitivity of CEST NMR Spectroscopy to Micro-to-Millisecond Dynamics in Nucleic Acids Using High-Power Radio-Frequency Fields. *Angew Chem Int Ed Engl* **59**, 11262-11266 (2020).
7. J. T. Baisden, J. A. Boyer, B. Zhao, S. M. Hammond, Q. Zhang, Visualizing a protonated RNA state that modulates microRNA-21 maturation. *Nat Chem Biol* **17**, 80-88 (2021).
8. D. M. Korzhnev, T. L. Religa, P. Lundstrom, A. R. Fersht, L. E. Kay, The folding pathway of an FF domain: characterization of an on-pathway intermediate state under folding conditions by (15)N, (13)C(alpha) and (13)C-methyl relaxation dispersion and (1)H/(2)H-exchange NMR spectroscopy. *J Mol Biol* **372**, 497-512 (2007).
9. P. Jemth, C. M. Johnson, S. Gianni, A. R. Fersht, Demonstration by burst-phase analysis of a robust folding intermediate in the FF domain. *Protein Eng Des Sel* **21**, 207-214 (2008).
10. P. Jemth *et al.*, Demonstration of a low-energy on-pathway intermediate in a fast-folding protein by kinetics, protein engineering, and simulation. *Proc Natl Acad Sci U S A* **101**, 6450-6455 (2004).
11. P. Vallurupalli, D. F. Hansen, P. Lundstrom, L. E. Kay, CPMG relaxation dispersion NMR experiments measuring glycine 1H alpha and 13C alpha chemical shifts in the 'invisible' excited states of proteins. *J Biomol NMR* **45**, 45-55 (2009).
12. V. P. Tiwari, S. Pandit, P. Vallurupalli, Exchangeable deuterons introduce artifacts in amide (15)N CEST experiments used to study protein conformational exchange. *J Biomol NMR* **73**, 43-48 (2019).

13. M. H. Levitt, Symmetrical Composite Pulse Sequences for Nmr Population-Inversion .2. Compensation of Resonance Offset. *J Magn Reson* **50**, 95-110 (1982).
14. M. Guenneugues, P. Berthault, H. Desvaux, A method for determining B_1 field inhomogeneity. Are the biases assumed in heteronuclear relaxation experiments usually underestimated? *J Magn Reson* **136**, 118-126 (1999).
15. T. Yuwen, L. E. Kay, G. Bouvignies, Dramatic Decrease in CEST Measurement Times Using Multi-Site Excitation. *Chemphyschem* **19**, 1707-1710 (2018).
16. T. Yuwen *et al.*, Measuring Solvent Hydrogen Exchange Rates by Multifrequency Excitation (15)N CEST: Application to Protein Phase Separation. *J Phys Chem B* **122**, 11206-11217 (2018).
17. F. Delaglio *et al.*, NMRPipe - a Multidimensional Spectral Processing System Based on Unix Pipes. *J Biomol NMR* **6**, 277-293 (1995).
18. T. D. Goddard, D. G. Kneller, *SPARKY 3 University of California, San Francisco* (2008).
19. W. Lee, M. Tonelli, J. L. Markley, NMRFAM-SPARKY: enhanced software for biomolecular NMR spectroscopy. *Bioinformatics* **31**, 1325-1327 (2015).
20. A. Ahlner, M. Carlsson, B. H. Jonsson, P. Lundstrom, PINT: a software for integration of peak volumes and extraction of relaxation rates. *J Biomol NMR* **56**, 191-202 (2013).
21. G. Bouvignies, *ChemEx (https://github.com/gbouvignies/chemex)* (2011).
22. H. M. McConnell, Reaction Rates by Nuclear Magnetic Resonance. *J Chem Phys* **28**, 430-431 (1958).
23. D. M. Korzhnev, T. L. Religa, W. Banachewicz, A. R. Fersht, L. E. Kay, A transient and low-populated protein-folding intermediate at atomic resolution. *Science* **329**, 1312-1316 (2010).
24. W. H. Press, B. P. Flannery, S. A. Teukolsky, W. T. Vetterling, *Numerical Recipes in C. The Art of Scientific Computing* (Cambridge University Press, Cambridge (UK), ed. Second Edition, 1992).
25. W. Y. Choy, Z. Zhou, Y. Bai, L. E. Kay, An 15N NMR spin relaxation dispersion study of the folding of a pair of engineered mutants of apocytochrome b562. *J Am Chem Soc* **127**, 5066-5072 (2005).
26. I. Bahar, R. Jernigan, K. A. Dill, *Protein actions : principles and modeling* (Garland Science, Taylor & Francis Group, New York, 2017), pp. xii, 322 pages.
27. P. Vallurupalli, N. Chakrabarti, R. Pomes, L. E. Kay, Atomistic picture of conformational exchange in a T4 lysozyme cavity mutant: an experiment-guided molecular dynamics study. *Chem Sci* **7**, 3602-3613 (2016).

28. J. T. Nielsen, F. A. A. Mulder, POTENCI: prediction of temperature, neighbor and pH-corrected chemical shifts for intrinsically disordered proteins. *J Biomol NMR* **70**, 141-165 (2018).